5th International Conference on Multiphase Flow, ICMF'04
Yokohama, Japan, May 30–June 4, 2004
Paper No. K07

Multi-Scale Modeling of Dispersed Gas-Liquid Two-Phase Flows

Niels G. Deen[1], Esther I.V. van den Hengel[1,2], Martin van Sint Annaland[1] and J.(Hans)A.M. Kuipers[1]

1: Faculty of Science and Technology, University of Twente, Enschede, The Netherlands, N.G.Deen@utwente.nl
2: TNO Prins Maurits Laboratory, Rijswijk, The Netherlands, Hengel@pml.tno.nl

Abstract In this work the status of computational modeling of bubbly flows is reviewed. The theory of four different models is introduced and typical examples are given illustrating the capabilities of these models. The volume of fluid model and the front tracking model are used to investigate the behavior of individual bubbles. It is found that both models are well suited to investigate the shape and transient behavior of individual bubbles. An Euler-Lagrange model is used to simulate the flow in a lab-scale bubble column, accounting for coalescence and break-up. The predicted bubble size distributions show reasonable agreement with experiments. However, better break-up models are necessary for further improvement. Finally an Euler-Euler model is used to simulate the flow in a lab-scale bubble column. It is shown that the use of a proper drag model is vital for accurate prediction of the bubble column dynamics.

1. Introduction

As bubble columns are widely used in the process industries, there is a need for reliable and practical models to describe the physical and chemical processes occurring in these systems. The complex interaction between mass transfer, fluid flow and chemical reactions in this type of process equipment makes the overall prediction of performance and scale-up very difficult. For this reason a lot of research has been devoted during the last decades to develop descriptive models based on first principles. Flows encountered in bubble columns are inherently unsteady (Sokolichin and Eigenberger, 1994) and display a wide range of time and length scales. As a direct consequence thereof we adopt a multi-scale modeling approach consisting of several levels (see Fig. 1) each developed to study the phenomena at a certain length scale, similar to the levels used in the work of Tomiyama (1998).

At the lowest level (i.e. the smallest time and length scale) we use the front tracking (FT) model originally developed by Tryggvason and co-workers (Unverdi and Tryggvason, 1992) and the volume of fluid (VOF) model to study the behavior of a single bubble or a few (interacting) bubbles. The idea is that simulations using the FT and VOF approach can generate insight in the behavior of a single rising gas bubble or the behavior of a few rising gas bubbles and provide closures for the bubble-liquid interaction. Due to the high computational load, these models can

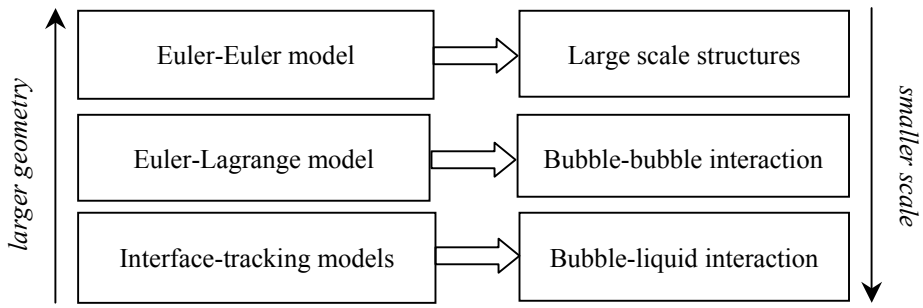

Fig. 1. Multi-level modeling concept for two-phase dispersed gas-liquid flows.

only be used for relatively small systems involving only a relatively small number of bubbles. The main difference between the VOF and FT models, is that the gas-liquid interface is represented in a different way. In the FT, the interface consists of a number of interconnected triangular segments of which the corner points are translated with the local interpolated fluid velocity. In VOF, the interface in each computational cell is reconstructed, through either a simple linear interface calculation (SLIC) or a piece-wise linear interface calculation (PLIC). Tomiyama (1998) used the former technique, while in this work the latter technique has been adopted.

For systems, at larger time and length scales we use the Euler-Lagrange (EL) or discrete bubble approach, which is particularly suited to study the effect of bubble-bubble and/or bubble-wall encounters. Because, contrary to the FT and VOF approach, the flow field at the scale of an individual bubble is not resolved, closure laws for bubble-liquid interaction (drag, lift and added mass forces) have to be provided.

At the largest time and length scales the Euler-Euler (EE) or continuum approach is used, which is particularly suited to model bubbly flows in industrial scale bubble columns. It can be considered as the workhorse for bubbly flow simulations in industry. Similar to the EL approach closures for bubble-liquid and bubble-bubble interactions have to be provided.

At the third international conference on multiphase flow, Tomiyama (1998) gave a clear view of his multi-level approach to computational modeling of bubbly flows. Tomiyama discussed the state-of-the-art models for bubbly flow together with several examples of work conducted in his group. It was shown that the volume of fluid (VOF) method is able to predict the shapes and rise velocities of individual bubbles in a quiescent liquid. Furthermore, the results of a 3D Euler-Lagrange model were presented. It was shown that for bubble sizes up to twice the computational grid size the model is able to predict important features of a bubble plume. Finally, Tomiyama demonstrated the features of an Euler-Euler model.

In this work, we would like to look back at the developments since the third international conference on multiphase flow and illustrate these through examples of work from our group. We will first briefly describe the theory of all models and then show example results of each of the models. Finally, some considerations for future work will be given.

2. Volume of fluid model and front tracking model

For incompressible flows the Navier-Stokes equations describing the fluid motion inside and outside the bubbles can be combined into a single vector equation for the fluid velocity **u** in the entire domain while accounting for the surface tension via a local volumetric force $\mathbf{F}_S$. Thus, the governing conservation equations for unsteady, incompressible, two material flows are given by:

$$\left(\nabla \cdot \mathbf{u}\right) = 0 \tag{1}$$

$$\frac{\partial}{\partial t}\left(\rho \mathbf{u}\right) + \left(\nabla \cdot \rho \mathbf{u}\mathbf{u}\right) = -\nabla p + \rho \mathbf{g} + \left(\nabla \cdot \mu\left[\left(\nabla \mathbf{u}\right) + \left(\nabla \mathbf{u}\right)^T\right]\right) + \mathbf{F}_S \tag{2}$$

where the local averaged density ρ and viscosity μ are evaluated from the local distribution of the indicator function F. For the local average density linear weighing of the gas and liquid densities is used:

$$\rho = F\rho_l + \left(1 - F\right)\rho_g \tag{3}$$

Usually the local average dynamic viscosity is also obtained via linear averaging of the gas and liquid dynamic viscosities. In this work an alternative, more fundamental approach recently

proposed by Prosperetti (2001) has been applied, where the local average viscosity is calculated via harmonic averaging of the kinematic viscosities:

$$\frac{\rho}{\mu} = F\frac{\rho_l}{\mu_l} + (1-F)\frac{\rho_g}{\mu_g} \tag{4}$$

The Navier-Stokes equations have been solved with a finite volume technique on a staggered rectangular three-dimensional grid using a two-step projection-correction method with an implicit treatment of the pressure gradient and explicit treatment of the convection and diffusion terms. A second order flux delimited Barton-scheme (Centrella and Wilson, 1984) has been used for the discretization of the convection terms and standard second order central finite differences for the diffusion terms. In order to be able to simulate systems with very large density ratios, the Navier-Stokes equations have been rewritten in their non-conservative form using the continuity equation,

$$\rho\left[\frac{\partial \mathbf{u}}{\partial t} + (\nabla\cdot\mathbf{uu})\right] = -\nabla p + \rho\mathbf{g} + \left(\nabla\cdot\mu\left[(\nabla\mathbf{u}) + (\nabla\mathbf{u})^T\right]\right) + \mathbf{F}_S \tag{5}$$

where $\mathbf{F}_S$ is the surface force, which is active at the gas-liquid interface. The density in the term on the left hand side has been evaluated at the old time level.

2.1 Surface tension

To model complex multiphase free surface flows a front tracking method based on direct numerical simulation has been introduced by Unverdi and Tryggvason (1992). Contrary to other numerical models developed to simulate multiphase flows, like the Level Set or Marker and Cell methods (Welch *et al.*, 1965) and Volume of Fluid methods (Nichols and Hirt, 1971; Youngs, 1982, 1987), the front tracking method uses an unstructured dynamic mesh to represent the interface surface and tracks this interface explicitly by the interconnected marker points. The Lagrangian representation of the interface avoids the necessity to reconstruct the interface from the spatial distribution of the fractions of the phases and, moreover, allows a direct calculation of the surface tension without the direct computation of the interface curvature, as is required in the Continuum Surface Force-method (CSF) introduced by Brackbill, Kothe, and Zemach (1992).

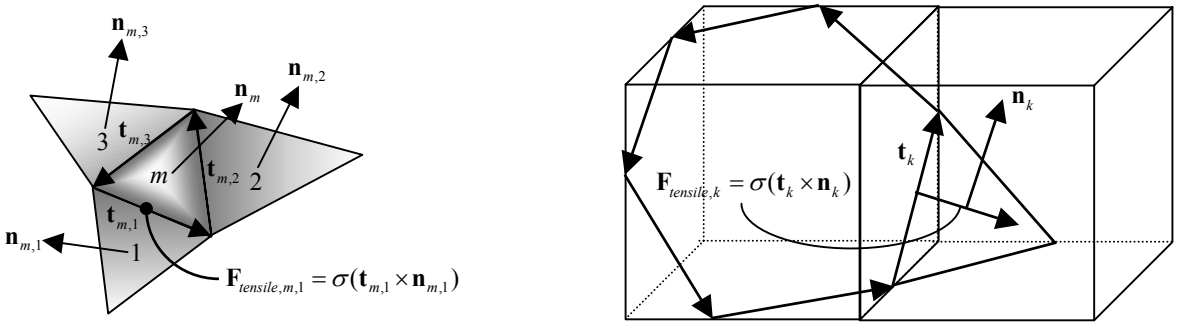

Fig. 2. Schematic representation of the calculation of the three tensile forces acting on the three edges of interface marker *m* in FT (left) and the tensile force acting on intersection *k* of the interface with a computational cell in VOF (right).

2.1.1 VOF model

In the VOF model, the force density, $\mathbf{F}_S$ is evaluated as follows:

$$\mathbf{F}_s = 2F\sigma\kappa\mathbf{n} = 2F\sigma(\mathbf{n}\times\nabla)\times\mathbf{n} \tag{6}$$

where $\mathbf{n}$ is the normal to the interface, which is computed from the gradient in the color function F:

$$\mathbf{n} = \nabla F \tag{7}$$

The calculation of $\mathbf{F}_S$ involves the second derivative with respect to F, which makes this formulation very sensitive to small numerical errors in the calculation of the liquid fraction. One way to prevent numerical problems, is to smooth the liquid fraction in Eqs. (6) and (7) with the use of a smoothing kernel D:

$$\tilde{F}(x,y,z)) = \sum_m D(x-x_m)D(y-y_m)D(z-z_m)F(x_m,y_m,z_m) \tag{8}$$

where D is the polynomial function suggested by Deen *et al.* (2004). In this study, Eqs. (6-8) were used for the calculation of the force density in the volume of fluid model.

2.1.2 FT model

In our implementation of the front tracking model, the problems associated with the evaluation of the second derivative of the phase fraction are circumvented by a direct calculation of the surface forces. Using the definition of the curvature, $\kappa\mathbf{n} = (\mathbf{n}\times\nabla)\times\mathbf{n}$, the surface force given in Eq. (6) for a interface element m can be rewritten as the contour integral of the tensile forces:

$$\mathbf{F}_{S,m} = \sigma\int_{\Delta s_m}\kappa\mathbf{n}_m ds_m = \sigma\int_{\Delta s_m}(\mathbf{n}_m\times\nabla)\times\mathbf{n}_m ds_m = \sigma\oint_{\Delta s_m}(\mathbf{t}_m\times\mathbf{n}_m)ds_m \tag{9}$$

where Δs_m is the area of the surface element, $\mathbf{t}_m$ is the counter clockwise unit tangent vector along the edges of the element and s is the length of these tangent vectors (i.e. the perimeter of the element), which is illustrated in Fig. 2. This method can be used on interface elements in both methods (Gunsing, 2004) and it leads to less numerical problems and a better accuracy, especially for cases involving large curvature.

After discretizing Eq. (9), the surface force can be distributed to the computational grid as follows:

$$\mathbf{F}_S(\mathbf{x}) = \frac{\sum_m\sum_\ell \rho_{m,\ell}D(\mathbf{x}-\mathbf{x}_{m,\ell})\sigma\left(\mathbf{t}_{m,\ell}\times\mathbf{n}_{m,\ell}\right)}{\sum_m\sum_\ell \rho_{m,\ell}D(\mathbf{x}-\mathbf{x}_{m,\ell})} \tag{10}$$

where $\mathbf{t}_{m,l}$ denotes the tangential vector to edge ℓ of marker m and D is the distribution kernel. Note that in this study the normal and tangent vectors of the edges of the elements are used, which can be obtained directly from the interface element data, in contrast to the method used by Tryggvason *et al.* (2001), where a polynomial fit for the interface is constructed from which the normal and tangent vectors to the elements are calculated. In order to avoid the distribution of the surface force to cells that have very low liquid volume fractions, which would result in large distortions of the

velocity field near the interface, a "mass weighing" function has been used to distribute the forces to the Eulerian grid (Deen *et al.*, 2004).

2.2 Calculation of the indicator function

The local distribution of the indicator function F is calculated in different ways in the two models. In the volume of fluid model, the advection of F is governed by:

$$\frac{DF}{Dt} = \frac{\partial F}{\partial t} + \mathbf{u} \cdot \nabla F = 0 \tag{11}$$

expressing that the interface property is advected with the local fluid velocity. That is to say that, given the orientation of the interface, the material fluxes through the cell faces are computed using geometrical advection. This pseudo-Lagrangian method offers the advantage that a very sharp interface is maintained during the simulation. An overview of the possible interface configurations is given in Fig. 3.

In the case of the front tracking model, F is computed from the location of the triangulated interface by solving a Poisson-equation, following the method proposed by Unverdi and Tryggvason (1992):

$$\nabla^2 F = \nabla \cdot \mathbf{G} = \nabla \cdot \sum_m D(\mathbf{x} - \mathbf{x}_m)\mathbf{n}_m \Delta s_m \tag{12}$$

where the summation is carried out over all markers m representing the interface, using $\mathbf{n}_m$ to denote the outwardly pointing normal on interface element m and Δs_m its surface area. The function D represents a numerical approximation of the Dirac-function normalized to the cell volume. In this work we used volume weighing. A robust Incomplete Cholesky Conjugate Gradient (ICCG) algorithm has been used to solve the Poisson-equation for the F-field.

The translation of the interface marker points deforms the triangular surface elements. To maintain an adequate resolution of the interface, the elements are reshaped in case the aspect ratio of the element edges becomes too large and elements are added or deleted in case the length of one of the edges becomes too large or too small compared to the Eulerian grid size, following Unverdi and Tryggvason (1992). In the simulations free slip boundary conditions were used for all confining walls.

3. Euler-Lagrange model

Our Euler-Lagrange model is based on the volume-averaged continuity and momentum equations given below to compute the liquid phase flow field.

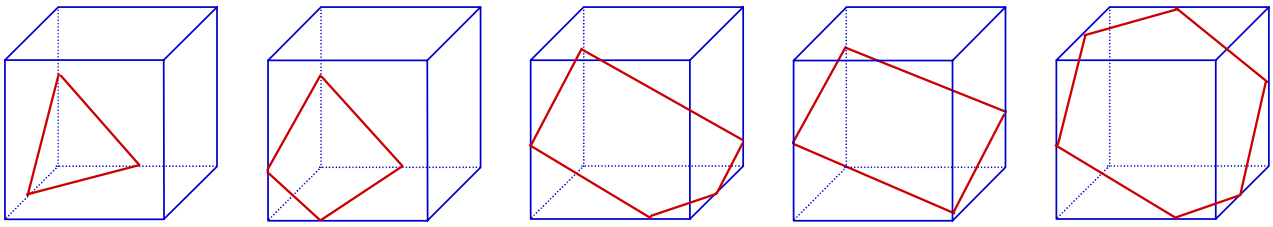

Fig. 3. Five generic types of interface configurations considered in the computation of the fluxes through the cell faces for the VOF model.

Table 1. Overview of interface forces used in the Euler-Lagrange model.

Interface force	*Expression*	*Closure*
Buoyancy	$\mathbf{F}_B = (\rho_g - \rho_l)\mathbf{g}V_b$	-
Drag	$\mathbf{F}_D = \frac{3}{4}\frac{C_D}{d_b}V_b\rho_l\left\|\mathbf{u}_l - \mathbf{w}_b\right\|(\mathbf{u}_l - \mathbf{w}_b)$	$C_D = \frac{2}{3}Eo^{\frac{1}{2}}$
Lift	$\mathbf{F}_L = C_L V_b \rho_l (\mathbf{u}_l - \mathbf{w}_b)\times(\nabla\times\mathbf{u}_l)$	$C_L = 0.5$
Virtual mass	$\mathbf{F}_{VM} = -\rho_l V_b C_{VM}\left(\frac{D_g\mathbf{w}_b}{Dt} - \frac{D_l\mathbf{u}_l}{Dt}\right)$	$C_{VM} = 0.5$

$$\frac{\partial}{\partial t}(\varepsilon_l\rho_l) + (\nabla\cdot\varepsilon_l\rho_l\mathbf{u}_l) = 0 \tag{13}$$

$$\frac{\partial}{\partial t}(\varepsilon_l\rho_l\mathbf{u}_l) + (\nabla\cdot\varepsilon_l\rho_l\mathbf{u}_l\mathbf{u}_l) = -\varepsilon_l\nabla p - (\nabla\cdot\varepsilon_l\tau_l) - \Phi_{l\to b} + \varepsilon_l\rho_l\mathbf{g} \tag{14}$$

The viscous stresses in the liquid phase are assumed to obey the general Newtonian form where the shear viscosity consists of the sum of a laminar and a turbulent contribution. Similar to the work of Deen *et al.* (2001) the latter is computed from a simple SGS turbulent viscosity model given by:

$$\mu_{l,\text{turbulent}} = \rho_l(C_s\Delta)^2\sqrt{\mathbf{S}^2} \tag{15}$$

where C_s equals 0.1, Δ represents the filter width and S the rate of strain tensor, respectively given by the following expressions:

$$\Delta = (\Delta x\Delta y\Delta z)^{1/3} \quad \text{and} \quad \mathbf{S}^2 = \frac{1}{2}\sum_i\sum_j\left(\frac{\partial u_i}{\partial x_j} + \frac{\partial u_j}{\partial x_i}\right)^2 \tag{16}$$

The ratio between the resolved and unresolved, sub-grid portion of the flow depends on the selected filter width, which in this case is linked to the size of the computational grid.

Two-way coupling is achieved via a source term, which can be computed from the positions and velocities of the bubbles. To obtain this information for each individual bubble the equation of motion is solved taking into account the action of external forces due to buoyancy, drag, lift and virtual mass:

$$\rho_g V_b\frac{d\mathbf{w}_b}{dt} = \mathbf{F}_B + \mathbf{F}_D + \mathbf{F}_L + \mathbf{F}_{VM} \tag{17}$$

The equations of the individual forces have been summarized in Table 1.

Discussion of these forces can be found in the work of Delnoij *et al*. (1997), Jakobsen *et al*. (1997), and Magnaudet and Eames (2000). Although shape parameters have an important influence on the rise velocity, as was illustrated by Tomiyama *et al.* (2002), we assumed the bubbles to be spherical in this work.

In our model encounters between a bubble and another bubble (binary encounter) and between a bubble and a solid wall have been accounted for. The processing of the bubble-bubble and bubble-wall encounters are evaluated as collisions between hard spheres and have been computed using an event driven computational strategy employing efficient techniques (such as the neighbourlist concept) taken from the field of Molecular Dynamics (MD) (see Delnoij *et al.*, 1997, and Delnoij,

1999 for further details).

Recently coalescence and breakup models were also included in the discrete bubble model (Van den Hengel 2004). Both the coalescence and breakup rates are modeled as the product of the collision frequency θ and respectively the coalescence or breakup efficiency λ:

$$Q(d_a, d_b) = \theta(d_a, d_b)\lambda(d_a, d_b) \tag{18}$$

In the event of coalescence, d_a and d_b are the diameters of the bubbles that are involved in the collision. The coalescence efficiency $\lambda(d_a, d_b)$ is the probability that coalescence occurs between two bubbles with diameter d_a and d_b once collision has occurred. The coalescence efficiency can be described as the fraction of bubbles that coalesce after collision, and depends on the ratio of the coalescence time and the contact time. The collision frequency $\theta(d_a, d_b)$ does not need to be modeled, as it is a result of the collisions, which are already accounted for.

In the case of breakup, the breakup efficiency is the probability that bubble *a* breaks after it 'hits' a liquid phase eddy *b*. The efficiency generally depends on the Weber number of the bubble. The collision frequency in Eq. (18) is modeled as the frequency that bubble *a* collides with eddy *b*, and depends on the turbulence intensity of the flow.

In our work we adopted the coalescence models of Chesters (1991) and Lee *et al.* (1987) and the breakup model of Luo and Svendsen (1996) in such way, that they can be applied to the discrete bubble model.

The boundary conditions and the numerical implementation details have already been described in the work of Delnoij *et al.* (1997). Details on the most recent improvements of the model can be found in the work of Darmana *et al.* (2004).

4. Euler-Euler model

In the two-fluid model the equations of motion of the dispersed gas-phase are filtered in order to obtain an Euler-Euler discription of the two-phase flow (e.g. Eqs. 13-14). Due to the filtering operation, unclosed parts emerge in the stress term and the interface forces. In this work, the unclosed part of the interface forces were neglected. The stress term was closed through an effective viscosity. The effective viscosity of the liquid phase is composed of a laminar, turbulent and bubble induced viscosity:

$$\mu_{eff,l} = \mu_{L,l} + \mu_{T,l} + \mu_{BIT,l} \tag{19}$$

The turbulent viscosity is calculated through Eq. (15), while the turbulence induced by the movement of the bubbles is accounted for with the model proposed by Sato (1975):

$$\mu_{BIT,l} = \rho_l C_{\mu,BIT} \alpha_g d_b \left| \mathbf{u}_g - \mathbf{u}_l \right| \tag{20}$$

with a model constant $C_{\mu,BIT}$ equal to 0.6.

The calculation of the effective gas viscosity was based on the effective liquid viscosity through:

$$\mu_{eff,g} = \frac{\rho_g}{\rho_l} \mu_{eff,l} \tag{21}$$

as was proposed by Jakobsen *et al.* (1997).

Table 2. Data used for VOF and FT simulations.

Property	*VOF and FT advection test*	*VOF spherical bubble*	*VOF ellipsoidal bubble*	*VOF skirted bubble*	*VOF skirted bubble*	*FT three bubbles*
Numerical grid	80x80x80	80x80x160	80x80x160	80x80x160	80x80x160	60x60x150
Grid size [m]	0.01	5.10^{-4}	5.10^{-4}	5.10^{-4}	1.10^{-4}	0.001
Time step [s]	0.001	1.10^{-5}	5.10^{-5}	5.10^{-5}	5.10^{-5}	1.10^{-4}
Bubble radius [m]	0.150	0.005	0.005	0.005	0.010	0.008
Liquid density [kg/m^3]	1000	1000	1000	1000	1000	1000
Liquid viscosity [kg/(m.s)]	0.1	0.6	0.316	0.1	0.1	0.1
Gas density [kg/m^3]	10	10	10	10	10	10
Gas viscosity [kg/(m.s)]	10^{-3}	6.10^{-3}	$3.16.10^{-3}$	10^{-3}	10^{-3}	10^{-3}
Surface tension [N/m]	0.1	1.0	0.01	0.01	0.01	1.0

The interface momentum transfer consists of forces due to drag, lift and virtual mass, which are summarized in Table 1. Note that these forces are given for individual bubbles. The volumetric force needed in the continuum model can simply be obtained by summing over all bubbles in the computational grid cell and dividing by the cell volume (i.e. replacing V_b by α_G).

The simulations are compared with experiments of Deen (2001), who performed two-camera particle image velocimetry (PIV) measurements in a 3-D bubble column filled with distilled water. The column had a square cross-section of 0.15 x 0.15 m^2 and a height of 1 m. The column was initially filled with water up to a height of 0.9 m. Air was introduced into the centre of the bubble column through a perforated plate at a superficial gas velocity of 4.9 mm/s.

5. Results

5.1 Volume of fluid model

As a first step, our VOF model was subjected to a test to verify its accuracy. We use a so-called standard advection test (Rider and Kothe 1998) in which basically the advection and reconstruction of the interface is tested in a prescribed flow field. We have conducted a rather severe test using a flow field in which considerable stretching and deformation of the interface occurs.

In addition to the test calculations computed shapes and rise velocities of gas bubbles were compared with the corresponding data obtained from the bubble diagram published by Grace (1973).

Following Rider and Kothe (1998), in our test a gas bubble was positioned in a box and subjected to a prescribed vortical flow field with corresponding stream function Ψ given by:

$$\Psi = \frac{1}{\pi}\sin^2(\frac{x}{a})\sin^2(\frac{y}{b}) \tag{22}$$

where a and b represent the box size in respectively the x- and y-direction (i.e. horizontal and vertical direction). The velocity components are related to the stream function Ψ by:

$$u_x = -\frac{\partial \Psi}{\partial y}; u_y = \frac{\partial \Psi}{\partial x}; u_z = 0 \tag{23}$$

By comparing the initial bubble shape with its shape obtained when the flow is advanced for n steps and then reversed for the same number of time steps the accuracy of our VOF model can be assessed. In Table 2 the data used for this test are summarized. In Fig. 4 the shape of the bubble is computed at several moments during the advection. A perfect computational technique would lead

to exactly the same spatial distribution of F-values at the beginning (Fig. 4a) and the end (Fig. 4c) of the integration process. Clearly small differences can be observed between the initial shape of the bubble and its final shape. A quantitative measure for the associated computational error E can be obtained from:

$$E = \frac{\sum_{i,j,k} \left| F_{i,j,k}^{end} - F_{i,j,k}^{initial} \right|}{\sum_{i,j,k} F_{i,j,k}^{initial}} \tag{24}$$

For our test E equals $1.04.10^{-3}$, which is in the same order of the results of the 2D calculations by Rider and Kothe (1998). The obtained value of E indicates that a relatively small error arises from the advection and reconstruction of the interface. Another important measure for the accuracy of the model, is the relative error in the bubble volume, E_{vol}:

$$E_{vol} = \frac{\sum_{i,j,k} F_{i,j,k}^{end} - \sum_{i,j,k} F_{i,j,k}^{initial}}{\sum_{i,j,k} F_{i,j,k}^{initial}} \tag{25}$$

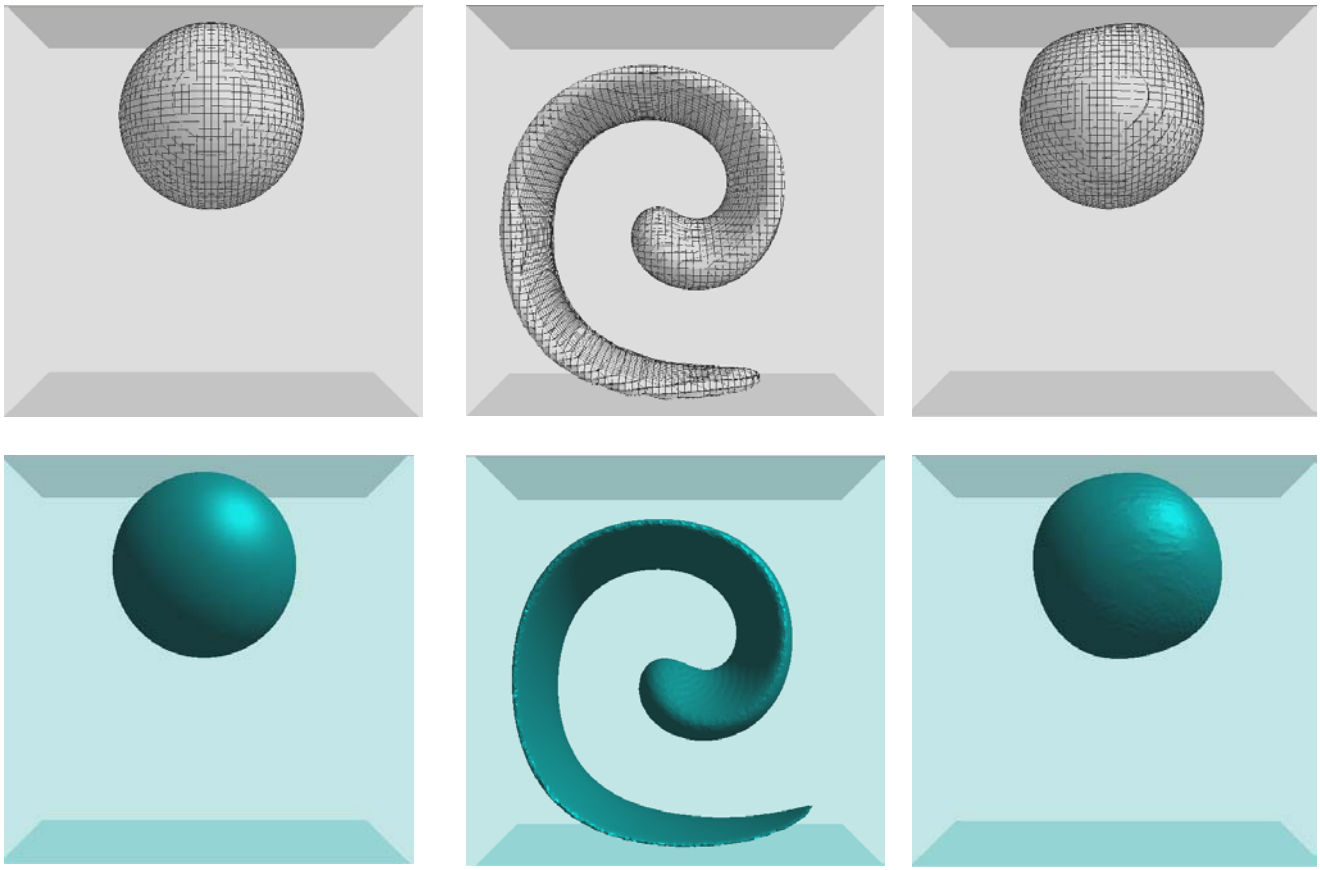

a. t = 0.0 s b. t = 1.0 s c. t = 0.0 s

Fig. 4. Bubble shapes computed by VOF (top row) and FT (bottom row) for the advection test: (a) initial bubble shape at t = 0.0 s, (b) bubble shape at the end of the forward integration in time at t = 1.0 s and (c) bubble shape at the end of the backward integration in time at t = 0.0 s.

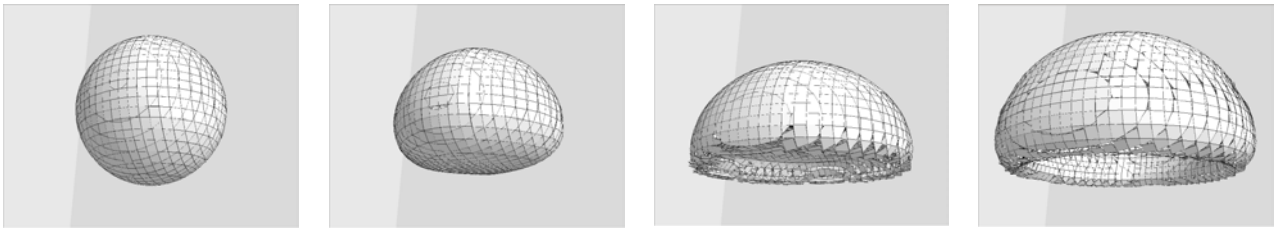

Spherical bubble	Ellipsoidal bubble	Large skirted bubble	Small skirted bubble
$Re_G = 1.7$, $Re_C = 1.61$	$Re_G = 4.6$, $Re_C = 4.30$	$Re_G = 20$, $Re_C = 18.2$	$Re_G = 60$, $Re_C = 52.4$

Fig. 5. Bubble shape and terminal rise velocities computed by the VOF for different bubbles. Re_G and Re_C represent respectively the bubble Reynolds number obtained from the Grace diagram and the computed bubble Reynolds number.

Note that this error only quantifies the accuracy of the volume conservation. For VOF E_{vol} is equal to $-7.0.10^{-6}$, which is extremely small.
From inspection of Fig. 4 and the computed E value it can be concluded that the advection and interface reconstruction algorithm work properly.

Another example of the capabilities of our model can be inferred from Fig. 5. In this figure the predicted shapes of several bubbles are shown. The properties of the simulation are given in Table 2. From Fig. 5 it is clear that our model is capable of predicting bubble shapes, at high density ratios and high values of the surface tension. The calculated rise velocities are in good agreement with the diagram of Grace (1973). It should be noted that in the presented figures the true interface representation is given and not the smoothed color function.

5.2 Front tracking model

The advection test as described in the previous section was also used to evaluate the accuracy of the front tracking model (see Fig. 4). The computational error E in this case is $4.3.10^{-3}$ and the error in the volume conservation E_{vol} is $-7.3.10^{-4}$. Both errors in the front tracking model are larger than with VOF, which can be attributed to the differences in the interface representation and the treatment of the volume fraction advection. Note that FT has a better interface representation, which can be seen from the sharper shape of the interface at $t = 1.0$ s. The VOF model on the other hand is inherently better in conserving the volume.

The interactions between several bubbles can be investigated with the Front Tracking model (Van Sint Annaland *et al.*, 2003). Results of a sample calculation, where three initially spherical bubbles were released in an initially quiescent liquid in a small column, are shown in Fig. 6. The bubbles are at initially at positions (0.015 m, 0.030 m, 0.015 m), (0.045 m, 0.030 m, 0.015 m) and (0.030 m, 0.030 m, 0.025 m). Firstly, the two lower bubbles on the left and right side are accelerated in the wake of the top bubble and almost catch up with the bubble in the centre (at t=0.15 s). Then, the two bubbles on both sides are pushed towards the free-slip walls, where they are again slowed down due to the downwards flowing liquid ($t = 0.25$ s).

5.3 Euler-Lagrange model

The Euler-Lagrange model was used to study the flow and bubble size distribution in a flat bubble column. The column has the dimensions of 0.20 x 0.03 x 1.40 m (W x D x H). The bottom of the column contains a membrane nozzle of 0.02 m, which was operated to yield a superficial gas velocity of 2.8 mm/s. Digital image analysis was used to measure the bubble size distribution at different heights in the column.

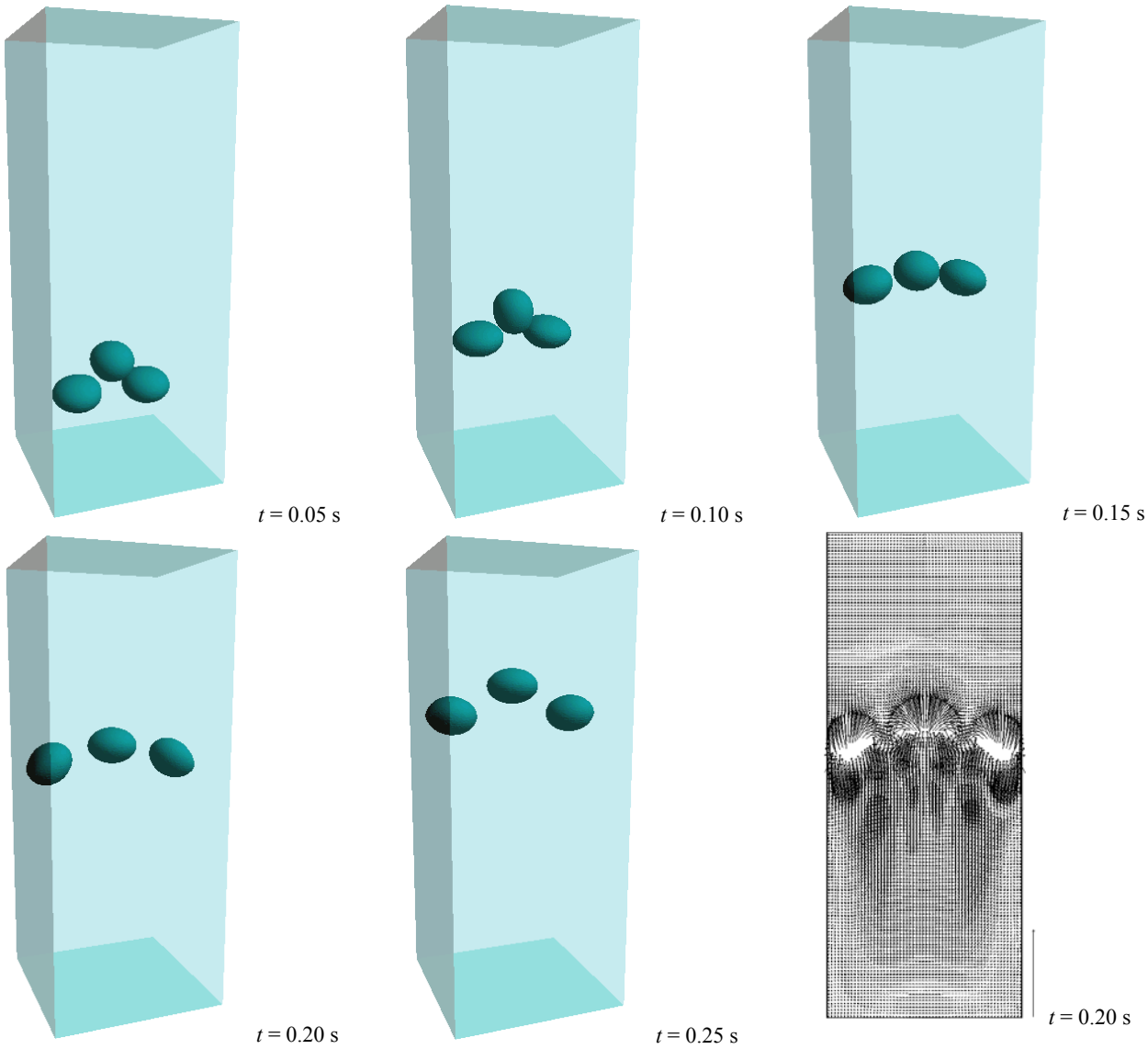

Fig. 6. Snapshots at different times of three initially spherical bubbles released in an initially quiescent liquid in a square column, calculated with the Front Tracking model. Also the velocity field at the central plane at t=0.20 s is shown (reference vector: 1.0 m/s). (Free-slip boundary conditions.)

The flow and the bubble size distribution was computed from the Euler-Lagrange model, which was described in section 3. In the simulations, the bubbles enter with a bubble size distribution around 3 mm, which is similar to that produced in the experiments. The grid of the computational domain consists of 20 x 3 x 140 cells and the time step is $1.0.10^{-3}$ s. Each case was simulated for 130 s. Two different coalescence models were used. In cases 1 and 2, the coalescence was modeled with the models of Chesters (1991) and Lee *et al.* (1987) respectively. In both cases the break-up model of Luo and Svendsen (1996) was used. A typical liquid velocity field and bubble configuration in the column is shown in Fig. 7. It was found that a bubble plume is formed at the inlet, which moves to the top of the column in a meandering fashion.

In this section the results of the simulations are discussed and compared with experimental data. We found that for the cases studied in this work, hardly any break-up occurs. This is due to the fact that the turbulence energy dissipation is very low in the studied column (i.e. in the order of 10^{-2} m^2/s^3). In systems for which the model of Luo and Svendsen (1996) was developed, the

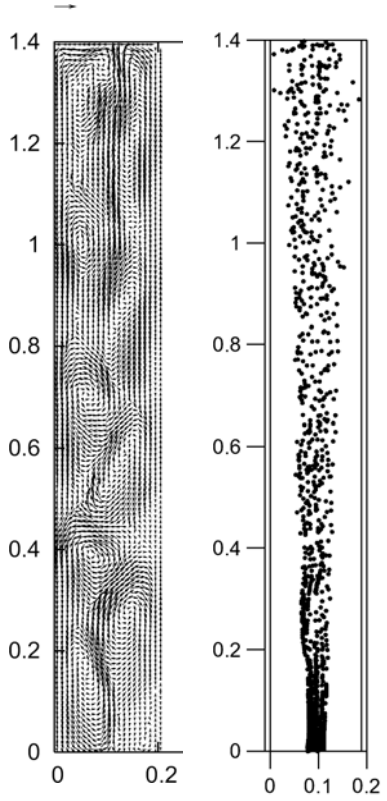

Fig. 7. Snapshots of the instantaneous liquid phase velocity field and the bubble positions simulated by the Euler-Lagrange model.

turbulence energy dissipation is much higher (i.e. larger than 0.5 m^2/s^3).

The simulation results of the two coalescence models are compared with the experimental results by means of the bubble size distribution. The Sauter mean diameter is calculated at four different heights in the column, as follows:

$$d_{32} = \frac{\sum_i d_i^3}{\sum_i d_i^2} \tag{26}$$

Close to the nozzle, the highest local gas hold-up is found. Subsequently most of the collisions and coalescence occurs in this portion of the column. In the upper part of the column the bubbles are more evenly spread and the chance for collision is smaller.

For the coalescence models of Chesters (1991) and Lee *et al.* (1987) we found that respectively 43% and 85 % of all collisions result in coalescence.

Fig. 8 shows the computed Sauter mean diameter as a function of the height in the column together with the experimental data. The mean diameter increases with increasing height in the column, because the higher their position in the column, the longer bubbles generally have resided in the column and the more opportunity they have had to coalesce. The increase in diameter can also be seen in the experiments. Both models overpredict the Sauter mean bubble diameter. This is probably due to the underestimation of the effects of break-up.

5.4 Euler-Euler model

The importance of the drag model in combination with the bubble size in the Euler-Euler model is illustrated by comparing two cases. In the first case, the bubble size is set to 4 mm and a drag model for large bubbles is used (see Table 1). In the second case, the bubble size is set to 2 mm and the standard drag relation given by Schiller and Nauman (1933) is used:

$$C_D = \frac{24}{\mathrm{Re}}(1 + 0.15\,\mathrm{Re}^{0.687}) \tag{27}$$

This relation is valid for solid spheres, but may also be applied for small bubbles in slightly contaminated water.

Both models were used to predict the hydrodynamics in a square cross-sectioned bubble column. Deen *et al.* (2001) performed two-camera particle image velocimetry (PIV) measurements of the gas and liquid velocities. The column has a square cross-section of 0.15 x 0.15 m^2 and a height of 1 m. The column was initially filled with water up to a height of 0.45 m. Air was

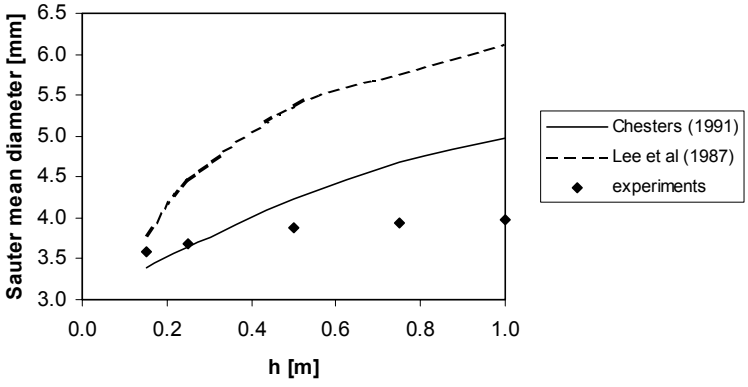

Fig. 8. Sauter mean diameter as a function of the height in the column.

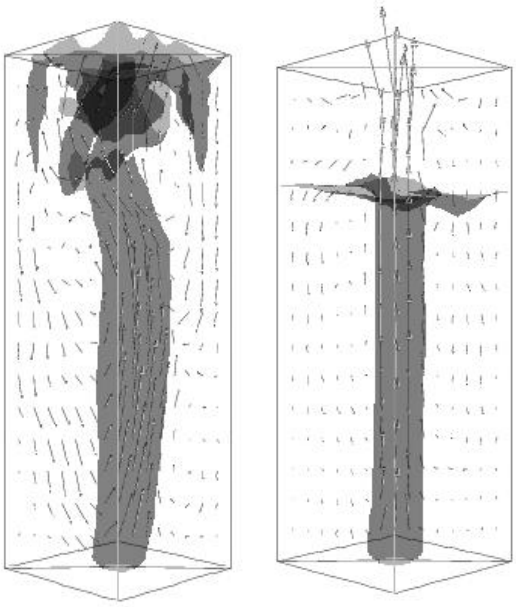

Fig. 9. Snapshots of the liquid phase velocity field and the instantaneous iso-surface of α_g = 0.03. Left: drag model large bubbles, right: drag model small bubbles.

introduced into the system through a perforated plate at a superficial gas velocity of 4.9 mm/s. The distributor plate contained 49 holes, with a diameter of 1 mm, which were positioned in the middle of the column at a square pitch of 6.25 mm. The bubble size observed in the experiments is about 4 mm in the middle of column.

Snapshots of the liquid phase velocity field and an iso-surface of the gas-fraction predicted by both models can be seen in Fig. 9. It is seen that the model with the drag closure for large bubbles predicts a transient solution. A bubble plume, which moves back and forth in the column in a random fashion, is observed in the simulation. The model with the drag closure for small bubbles, on the other hand, does not predict this behavior. Instead, a quasi steady state solution is obtained, which is in disagreement with the experimental observations of Deen *et al.* (2001).

A more quantitative comparison between the two drag models can be obtained from Fig. 10. This figure shows time-averaged profiles of the vertical liquid velocity and the horizontal and vertical fluctuations at a height of 0.25 m in the column. It is observed that the drag model for the large bubbles yields a much better agreement with the experimental data, than that for the small bubbles. In the latter case the drag force is seriously underestimated, yielding a bubble plume which rises straight to the top of the column, only causing liquid movement in the vicinity of the bubble plume.

6. Conclusions

In this paper the multi-level modelling approach for dispersed gas-liquid two-phase flows has been introduced and discussed. The four models constituting this approach, namely the volume of fluid model, the front tracking model, the Euler-Lagrange and the Euler-Euler model, have been shortly described and corresponding illustrative computational results have been presented.

To resolve the flow phenomena at the lowest level a fully 3D volume of fluid model has been developed, which can handle systems with very high density ratios and very high surface tension coefficients. Computed bubble shape and bubble rise velocity for a single bubble rising in a liquid compared well with experimental data (Grace, 1973) for several selected cases with different bubble sizes.

Furthermore, results of a front tracking calculation with three bubbles was shown to demonstrate the capabilities of the front tracking model to study bubble-wake interactions.

At the intermediate level the Euler-Lagrange model has been used, which allows accounting for coalescence and break-up. It is found that the break-up model predicts hardly any break-up for the homogeneous flow regime, which has been investigated in this work.

At the highest level the Euler-Euler approach has been applied to study the effect of closures for gas-liquid interaction. It has been shown that a proper use of the bubble size and the related drag model is vital in a correct prediction of the prevailing hydrodynamics.

One of the unresolved issues is that the drag force depends on the bubble shape, which in turn is a function of the strength of the local shear field. In order to incorporate this information into the closure relations, a parameter study of the bubble size and the shear field is required. These calculations require a considerable computational effort, which has not been carried out yet. Another aspect that needs further attention is the hydrodynamic interaction between bubbles. When bubbles move in swarms, the liquid flow field is altered considerably, which results in altered closure relations. The front tracking method is particularly suited to investigate this effect, since this method does not suffer from unphysical numerical coalescence. That is to say, techniques like volume of fluid (VOF) cannot handle the presence of the interfaces of two bubbles in one grid cell. When such a situation occurs, the gas fractions of these two bubbles will be merged and coalescence follows automatically. Contrary to VOF, front tracking does not allow for coalescence, unless a physical sub-grid scale model is explicitly implemented. The front tracking method can be used to quantify the force coefficients as a function of the mean free path of the bubbles or the local gas fraction. The former is best suited for use in Euler-Lagrange simulations, because the position and therefore the mean free path of each bubble are known. The latter can be used in Euler-Euler models, because in these models only the local gas fraction is known.

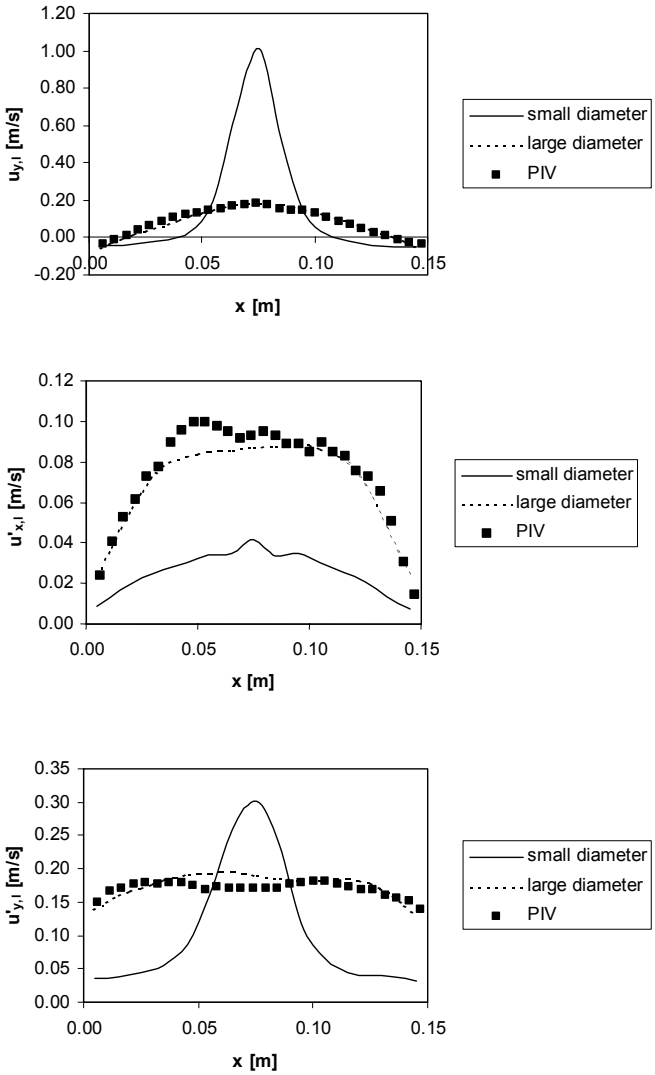

Fig. 10. Comparison of the simulated and experimental average liquid velocity profiles for two different drag models at a height of 0.25 m and a depth of 0.075 m. Top: average liquid velocity; middle: vertical liquid velocity fluctuations; bottom: horizontal liquid velocity fluctuations.

References

Brackbill, J. U., Kothe, D. B. & Zemach, C., 1992. A continuum method for modeling surface tension. Journal of Computational Physics, 100, 335-354.

Centrella, J. & Wilson, J., 1984. Planar numerical cosmology. II. The difference equations and numerical tests, Astrophysical Journal Supplement Series, 54, 229-249.

Chesters, A.K., 1991. The modelling of coalescence processes in fluid-liquid dispersions: a review of current understanding, Transactions of IChemE, 69, 259-270.

Darmana, D., Deen, N.G., Kuipers, J.A.M., 2004. Detailed Modeling of Hydrodynamics, Mass transfer and Chemical Reactions in a Bubble Column using a Discrete Bubble Model, in preparation.

Deen, N. G., 2001. An experimental and computational study of fluid dynamics in gas-liquid chemical reactors, Ph.D. thesis, Aalborg University Esbjerg.

Deen, N. G., Solberg, T. & Hjertager, B. H., 2001. Large Eddy Simulation of the Gas-Liquid Flow in a Square Cross-sectioned Bubble Column. Chemical Engineering Science, 56, 6341-6349.

Deen N. G., van Sint Annaland, M., & Kuipers, J. A. M., 2004. Multi-scale Modeling of Dispersed Gas-Liquid Two-Phase Flow. Chem. Eng. Sci., accepted for publication.

Delnoij, E. Lammers, F.A., Kuipers, J.A.M. & van Swaaij, W.P.M., 1997. Dynamic simulation of dispersed gas-liquid two-phase flow using a discrete bubble model. Chemical Engineering Science, 52(9), 1429-1458.

Delnoij, E., 1999. Fluid dynamics of gas-liquid bubble columns: A theoretical and experimental study, Ph.D. thesis, Twente University, The Netherlands.

Grace, J.R., 1973. Shapes and velocities of bubbles rising in infinite liquids. Transactions Institute Chemical Engineers, 51, 116-120.

Gunsing, M., 2004. Modelling bubbly flows using volume of fluid, front tracking and discrete bubble models, Ph.D. thesis, Twente University, The Netherlands.

Jakobsen, H.A., Sannaes, B.H., Grevskott, S. & Svendsen, H.F., 1997. Modeling of vertical bubble-driven flows. Industrial and Engineering Chemistry Research, 36, 4052-4074.

Lee, C.-H., Erickson, L.E., Glasgow, L.A., 1987. Bubble breakup and coalescence in turbulent gas-liquid dispersion, Chemical Engineering Communications, 59, 65-84.

Luo, H. and Svendsen, H.F., 1996. Theoretical model for drop and bubble breakup in turbulent dispersions, AIChE Journal, 42, 1225-1233.

Magnaudet, J. & Eames, I., 2000. The motion of high-Reynolds-number bubbles in inhomogeneous flows. Annual Reviews in Fluid Mechanics, 32, 659-708.

Nichols, B.D. & Hirt, C.W., 1971. Improved free surface boundary conditions for numerical incompressible-flow calculations, Journal of Computational Physics, 8, 434-448.

Prosperetti, A., 2001. Navier-Stokes numerical algorithms for free-surface flow computations: An overview. Drop Surface Interactions, 21.

Rider, W.J. and Kothe, D.B. 1998. Reconstructing volume tracking, Journal of Computational Physics, 141, 112-152.

Sato, Y. & Sekoguchi, K., 1975. Liquid velocity distribution in two-phase bubble flow, International Journal of Multiphase Flow, 2(1), 79-95.

Schiller, L. and Nauman, A., 1933. A drag coefficient correlation, VDI Zeitschrift, 77, 318-320

Sokolichin, A. & Eigenberger, G., 1994. Gas-liquid flow in bubble columns and loop reactors: part I. Detailed modelling and numerical simulation, Chemical Engineering Science, 49(24), 5735-5746.

Tomiyama, A., 1998. Struggle with Computational Bubble Dynamics. Third International Conference on Multiphase Flow, Lyon, France, June 8-12, 1998.

Tomiyama, A., Tamai, H., Zun, I. & Hosokawa, S., 2002. Transverse migration of single bubbles in simple shear flows, Chemical Engineering Science, 57, 1849–1858.

Tomiyama, A., Celata, G. P., Hosokawa, S., & Yoshida, S., 2002. Terminal velocity of single bubbles in surface tension force dominant regime. International Journal of Multiphase Flow, 28, 1497-1519.

Tryggvason, G., Bunner, B., Esmaeeli, A., Juric, D., Al-Rawahi, N., Tauber, W., Han, J., Nas, S. & Jan, Y.J., 2001. A front tracking method for the computations of multiphase flow. Journal of Computational Physics, 169, 708-759.

Unverdi, S.O. & Tryggvason, G., 1992. A front-tracking method for viscous, incompressible multi-fluid flows. Journal of Computational Physics, 100, 25-37.

Van den Hengel, E.I.V., 2004. Multi-level modeling of gas-liquid two-phase flow in a bubble column, Ph.D. thesis, Twente University, The Netherlands.

Van Sint Annaland, M., Deen N. G., & Kuipers, J. A. M., 2003. Multi-Level Modelling of Dispersed Gas-Liquid Two-Phase Flows. Series: Heat and Mass Transfer. Editors: M. Sommerfeld and D. Mewes, Springer-Verlag, 139-157.

Welch, J.E., Harlow, F.H., Shannon, J.P. & Daly, B.J., 1965. The MAC method: a computing technique for solving viscous incompressible transient fluid flow problems involving free surfaces. Los Alamos Scientific Laboratory Report LA-3425.

Youngs, D.L., 1982. Time-dependent multi-material flow with large fluid distortion, In: Numerical methods for fluid dynamics, K.W. Morton & M.J. Baines (Eds.), Academic Press, New York, 273.

Youngs, D.L., 1987. An interface tracking method for a 3D Eulerian hydrodynamics code. Technical Report AWRE/44/92/35. Atomic Weapons Research Establishment, April 1987.